A Graphene-Supported Single-Atom FeN$_5$ Catalytic Site for Efficient Electrochemical CO$_2$ Reduction

Huinian Zhang[+], Jing Li[+], Shibo Xi, Yonghua Du, Xiao Hai, Junying Wang, Haomin Xu, Gang Wu, Jia Zhang,* Jiong Lu,* and Junzhong Wang*

Abstract: *Electrochemical conversion of CO$_2$ into valued products is one of the most important issues but remains a great challenge in chemistry. Herein, we report a novel synthetic approach involving prolonged thermal pyrolysis of hemin and melamine molecules on graphene for the fabrication of a robust and efficient single-iron-atom electrocatalyst for electrochemical CO$_2$ reduction. The single-atom catalyst exhibits high Faradaic efficiency (ca. 97.0%) for CO production at a low overpotential of 0.35 V, outperforming all Fe-N-C-based catalysts. The remarkable performance for CO$_2$-to-CO conversion can be attributed to the presence of highly efficient singly dispersed FeN$_5$ active sites supported on N-doped graphene with an additional axial ligand coordinated to FeN$_4$. DFT calculations revealed that the axial pyrrolic nitrogen ligand of the FeN$_5$ site further depletes the electron density of Fe 3d orbitals and thus reduces the Fe–CO π back-donation, thus enabling the rapid desorption of CO and high selectivity for CO production.*

Electrochemical reduction of carbon dioxide (CO$_2$) to gaseous fuels or energy-dense liquids offers a promising strategy for both storing energy and managing the global carbon balance.[1] However, the practical implementation of this technique is highly challenging owing to the chemical inertness of CO$_2$ and the multiple electron- and proton-transfer processes involved for its transformation into numerous products.[2] Of all products, carbon monoxide (CO) is emerging as one of the most practical targets because of its large current density and the high selectivity as compared to other CO$_2$ reduction routes.[3] Moreover, CO$_2$-to-CO conversion also represents a key step in Fischer–Tropsch processes towards the preparation of synthetic fuels. In this regard, robust and efficient electrocatalysts must be developed to mediate the electron- and proton-transfer steps to favor CO production over the competing hydrogen evolution reaction.

Over the past few decades, numerous noble-metal electrocatalysts have been reported for CO$_2$-to-CO conversion, including Cu,[4] Ag,[5] and Au.[6] However, inadequate activity and selectivity associated with these catalysts are prohibitive for their practical application. Therefore, the transition to earth-abundant nonprecious metals for the electrocatalytic reduction of CO$_2$ to CO is highly desirable. Recently, single non-noble-metal atoms embedded in N-doped carbon supports have been proposed and reported to be highly efficient electrocatalysts for the CO$_2$-to-CO transformation under aqueous conditions.[7] The unique electronic structure of these single-metal active sites with maximized atomic efficiency render them promising electrocatalysts for the CO$_2$ reduction reaction (CO$_2$RR). Despite rapid progress in this field, the rational development of robust electrocatalysts with well-defined single-atom active sites to boost the catalytic performance for CO$_2$RR still remains a significant challenge.

In this study, we developed a facile approach for the synthesis of a single-atom catalyst (SAC) consisting of atomically dispersed FeN$_5$ active sites supported on N-doped graphene for efficient CO$_2$RR. The FeN$_5$ SAC was synthesized through the thermal pyrolysis of hemin (H) and melamine (M) coadsorbed on graphene (G). On one hand, such a codeposition strategy allows the cross-linking of hemin and melamine at elevated temperatures, which effectively suppresses the aggregation of iron atoms on graphene during the thermal annealing process. On the other hand, the melamine provides a rich nitrogen source to introduce the N-dopant into graphene and to anchor an individual iron atom for the formation of a unique FeN$_5$ active site. The presence of graphene not only increases the electrical conductivity of the as-synthesized catalyst, but also creates hierarchical porosity with an enhanced specific surface area. The resultant SAC exhibited a high CO Faradaic efficiency

[*] H. Zhang,[+] Prof. J. Wang
    Institutes of Physical Science and Information Technology
    Key Laboratory of Structure and Functional Regulation of Hybrid
    Materials of Ministry of Education, Anhui University
    Hefei 230601 (P. R. China)
    E-mail: wangjz@ahu.edu.cn

    H. Zhang,[+] J. Wang, Prof. J. Wang
    CAS Key Laboratory of Carbon Materials, Institute of Coal Chemistry
    Chinese Academy of Sciences
    Taiyuan 030001 (China)

    J. Li,[+] X. Hai, H. Xu, Prof. J. Lu
    Department of Chemistry, National University of Singapore
    3 Science Drive 3, Singapore 117543 (Singapore)
    E-mail: chmluj@nus.edu.sg

    S. Xi, Y. Du
    Institute of Chemical and Engineering Sciences
    Pesek Road, Jurong Island, 627833 Singapore (Singapore)

    G. Wu, J. Zhang
    Institute of High Performance Computing
    A*STAR (Agency for Science, Technology and Research)
    1 Fusionopolis Way, #16-16 Connexis S138632 (Singapore)
    E-mail: zhangj@ihpc.a-star.edu.sg

    J. Wang
    Dalian National Laboratory for Clean Energy
    Dalian 116023 (China)

[+] These authors contributed equally to this work.

Supporting information and the ORCID identification number(s) for
the author(s) of this article can be found under:
https://doi.org/10.1002/anie.201906079.

(ca. 97.0%) at a low overpotential of 0.35 V, thus outperforming all Fe-N-C-based catalysts. We expect that our findings will accelerate the development of novel SACs with tunable local structures for efficient electrochemical transformations beyond CO_2 reduction.

To create atomically dispersed FeN_5 sites embedded in the N-doped graphene matrix, we designed the following synthetic strategy using a prolonged thermal pyrolysis method. Hemin (ferric chloride heme) was selected as the iron source owing to the presence of ferric iron (Fe^{3+}) bonded to the tetrapyrrole macrocycle and two propionic acid groups (-CH_2-CH_2-COOH). As illustrated in Figure 1, the first step
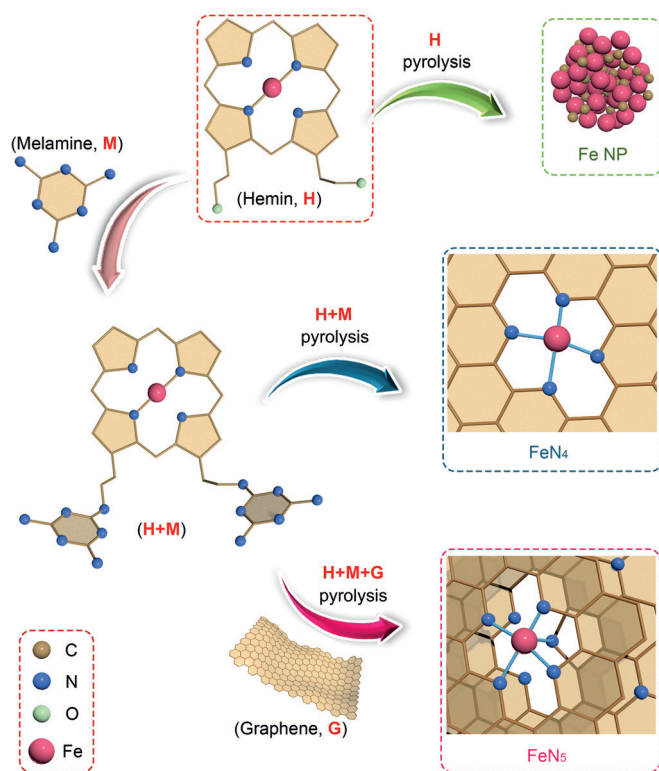

Figure 1. Synthetic route towards single-atom FeN_4 and FeN_5 catalysts.

involves gentle thermal treatment (ca. 200°C) of H mixed with M to trigger their cross-linking (H–M) through a dehydration reaction between the carboxy group (-COOH) of H and the NH_2 group of M. Subsequently, prolonged thermal pyrolysis (at a rate of 2°C min^{-1} up to 800°C) was expected to create the catalyst consisting of isolated FeN_4 structures embedded in the carbon matrix. In contrast, a single hemin source upon thermal annealing tends to form iron-based nanoparticles Fe NP with few single Fe-N$_x$ sites. Upon the addition of defective graphene with an excess amount of M, thermal decomposition of M at high temperature results in the formation of N-doped graphene. The N-dopant forms an additional axial ligand coordinated with FeN_4 to form a new FeN_5 catalytic site anchored on graphene (H-M-G, Figure 1, bottom right). The morphology and phase of various samples were characterized by X-ray diffraction (XRD), SEM, and TEM (see Figures S1–S3 in the Supporting Information). We

also conducted in situ FTIR measurements to monitor the change in hemin and melamine on graphene as a function of annealing temperature (see Figure S4). The gradual decrease in intensity of the peaks associated with the amine (around 3600 cm^{-1}) and carboxy groups (1715–1720 cm^{-1}) in H-M reveals a possible amidation reaction between H and M, which favors the formation of atomically dispersed single Fe sites.

We first conducted spherical-aberration-corrected scanning transmission electron microscopy–annular dark field (STEM-ADF) measurements to gain a detailed understanding of the morphologies of as-prepared catalysts (derived from H-M-G). A large-field-of-view STEM-ADF image showed an absence of larger clusters of as-prepared catalyst (H-M-G; Figure 2a). An atomic-resolution STEM-ADF image (Figure 2b) revealed that Fe atoms were atomically dispersed and well-separated on graphene without aggregation into particles. We also carried out electron energy loss spectroscopy (EELS) measurements of this sample. The EELS spectrum (Figure 2c) acquired in the region marked by the dashed rectangle in Figure 2a revealed the coexistence of Fe $L_{2,3}$-edge and N K-edge features, with peaks at 708.0 and 401.6 eV, thus suggesting that isolated Fe atoms were probably anchored in graphene through bonding with nitrogen atoms. The observation of a weak oxygen-related signal is presumably due to the presence of COOH groups in the H molecule. The surface atomic concentration of Fe and N in the H-M-G sample was determined by X-ray photoemission
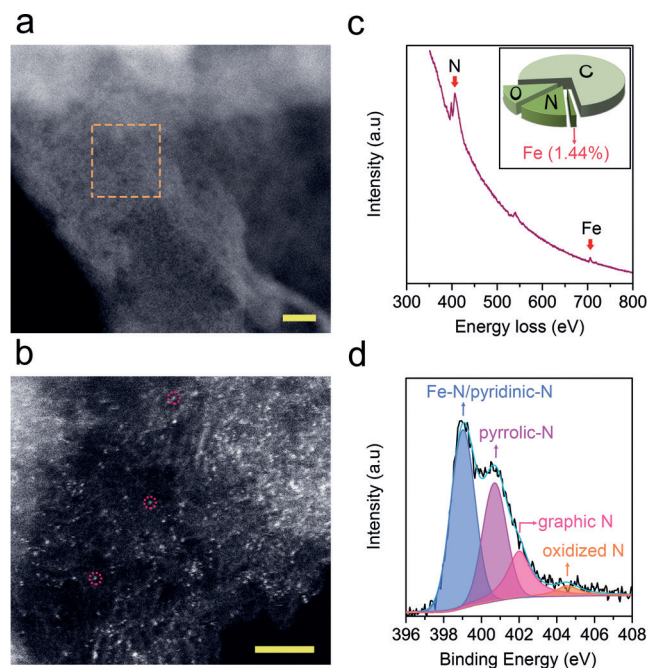

Figure 2. Morphology and compositional characterization of the FeN_5 catalyst (H-M-G). a) Large-field of view and b) magnified view of STEM images of uniformly distributed single Fe atoms in graphene. Dashed circles in (b) indicate typical single Fe atoms. Scale bars: 10 nm (a), 2 nm (b). c) EELS spectra of the N K-edge, O K-edge, and Fe $L_{2,3}$-edge as acquired in the catalyst region marked by dashed rectangle in (a). The inset reveals the corresponding elemental ratio derived from XPS data. d) High-resolution N 1s XPS spectra for the H-M-G catalyst.

spectroscopy (XPS) to be 1.44 and 13.56%, respectively (Figure 2c, inset), which is higher than that in the H-G catalyst (Fe 0.87%, N 1.65%; see Figure S5), thus indicating that the use of melamine not only facilitates the N-doping of graphene but also favors the subsequent coordination to anchor iron atoms. Furthermore, the high-resolution N 1s spectrum of the H-M-G sample (Figure 2d; see also Figure S6) can be deconvoluted into four components corresponding to pyridinic N or Fe-N (centered at 399.0 eV), pyrrolic N (400.8 eV), graphitic N (401.9 eV), and oxidized N (404.8 eV).[8] The coexistence of a high percentage of pyridinic and pyrrolic N plays an important role for the formation of unique FeN_5 sites towards the efficient CO_2RR, as discussed below.

To probe the local structural and electronic states of the Fe atoms, we performed X-ray absorption near edge structure (XANES) measurements of as-synthesized catalysts. The edge of XANES spectra of both H-M (FeN_4) and H-M-G (FeN_5) samples shifted towards higher binding energy as compared to that of Fe foil (Figure 3a), thus suggesting a positive charge state of Fe atoms in the as-prepared catalysts (H-M and H-M-G).[9] Additional structural information can also be inferred from extended X-ray adsorption fine structure (EXAFS) spectra at the Fe K-edge (Figure 3d). Furthermore, the Fourier transformed (FT) $k^2\chi(k)$ spectrum exhibited a dominant peak centered around 1.47 and 1.56 Å for the H-M and H-M-G sample, respectively. The absence of the peak at approximately 2.18 Å (corresponding to the Fe−

Fe bond) further confirms the atomic dispersion of isolated Fe atoms in these two samples.[10] In contrast, the Fourier transformed (FT) $k^2\chi(k)$ spectrum of the H sample shows two features at 1.56 and 2.18 Å, suggesting the coexistence of isolated Fe sites and Fe nanoparticles.

We performed DFT calculations in combination with a standard XANES calculation method to determine the atomic structures of the iron single-atom catalysts (Fe_1-SACs). On the basis of the plausible reaction mechanism and all the observations discussed above, it is most likely that isolated FeN_4 and FeN_5 sites are formed in H-M and H-M-G, respectively. These two proposed configurations for the Fe_1-SACs synthesized in this study were further optimized by DFT calculations (see Figure S7 and Table S1 in the Supporting Information). To verify these two structures, we calculated their corresponding XANES spectra (Figure 3b,c) using the finite difference method of the FDMNES code,[11] which showed good agreement with our experimental data acquired on the H-M and H-M-G catalyst, respectively, thus indicating that we successfully synthesized two types of Fe_1-SACs: FeN_4 for H-M and FeN_5 for H-M-G.

An excess of melamine (M) assists the formation of separated $Fe-N_4$ sites in the H-M sample through thermal annealing. In contrast, the addition of defective graphene to H and M facilies the formation of FeN_5 rather than FeN_4 sites. The graphene sheet will be subjected to N-doping at high temperature in the presence of a large amount of M. The resulting N-doped graphene provides the axial ligand site for coordination with FeN_4 to create a new FeN_5 site. The introduction of a high density of N-dopants in this H-M-G sample is further supported by the EDS and Raman spectra. EDS analysis (see Figure S8) showed that the amount of N atoms (16.5 atom%) was approximately 20 times higher than the amount of Fe atoms (0.8 atom%) in the H-M-G sample, thus indicating an abundance of N sites for the formation of pentacoordinated iron (FeN_5). Analysis of the intensity ratio of the D (1360 cm^{-1}) and G bands (1590 cm^{-1}) in Raman spectra allows us to probe the degree of disorder in graphitic systems (see Figure S9e). The I_D/I_G ratios of H-M-G and H-M were determined to be 1.06 and 1.13, respectively, and thus much higher than for graphene (0.4), as attributed to the formation of a high density of N-dopant and embedded single Fe atoms in these samples.

After gaining a better understanding of the structure of these samples, we evaluated their electrocatalytic performance for CO_2RR using a two-compartment electrochemical cell in 0.1M $KHCO_3$ solution. The linear sweep voltammetry (LSV) measurements of the FeN_5 catalyst in both CO_2- and Ar-saturated 0.1M $KHCO_3$ are shown in Figure 4a. For a CO_2-saturated $KHCO_3$ solution, CO_2RR was initiated at a potential of −0.26 V (vs. RHE), corresponding to an overpotential of 0.15 V (note that the equilibrium potential for the CO_2/CO couple is −0.11 V (vs. RHE) at pH 6.8[12]). The resulting current density increased abruptly below −0.40 V, as attributed to the CO_2RR together with the competing HER.

We employed gas chromatography (GC) and ^1H NMR spectroscopy to analyze the gaseous and liquid products from CO_2RR using different catalysts. It was observed that CO was the dominant product; liquid product was absent for all the
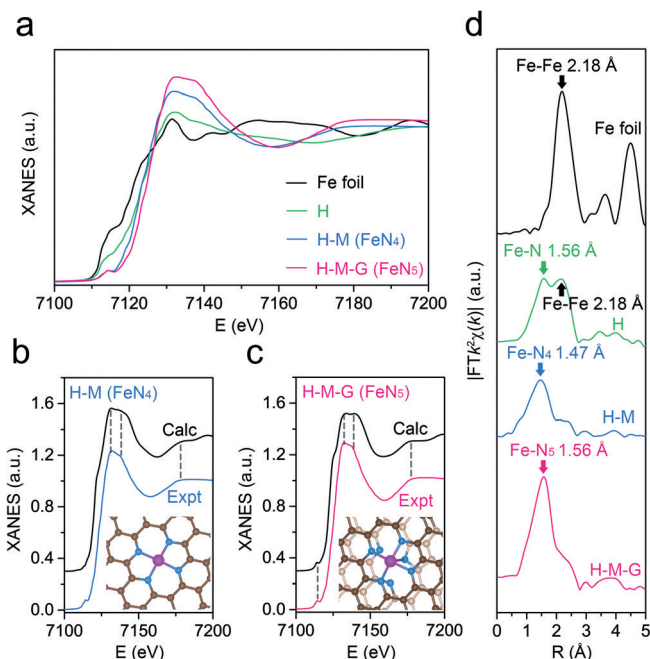

Figure 3. Fe K-edge XANES and EXAFS spectra of different samples. a) Experimental Fe K-edge XANES spectra of synthesized catalysts and Fe foil. b,c) Comparison of the experimental XANES curves with the calculated XANES data of FeN_4 (pyrolyzed sample of hemin and melamine molecules, H-M) and FeN_5 (pyrolyzed sample of hemin and melamine on graphene, H-M-G). The insets show the DFT-optimized FeN_4 and FeN_5 structure, respectively. d) Fourier transformed (FT) extended X-ray absorption fine structure (EXAFS) of these samples.
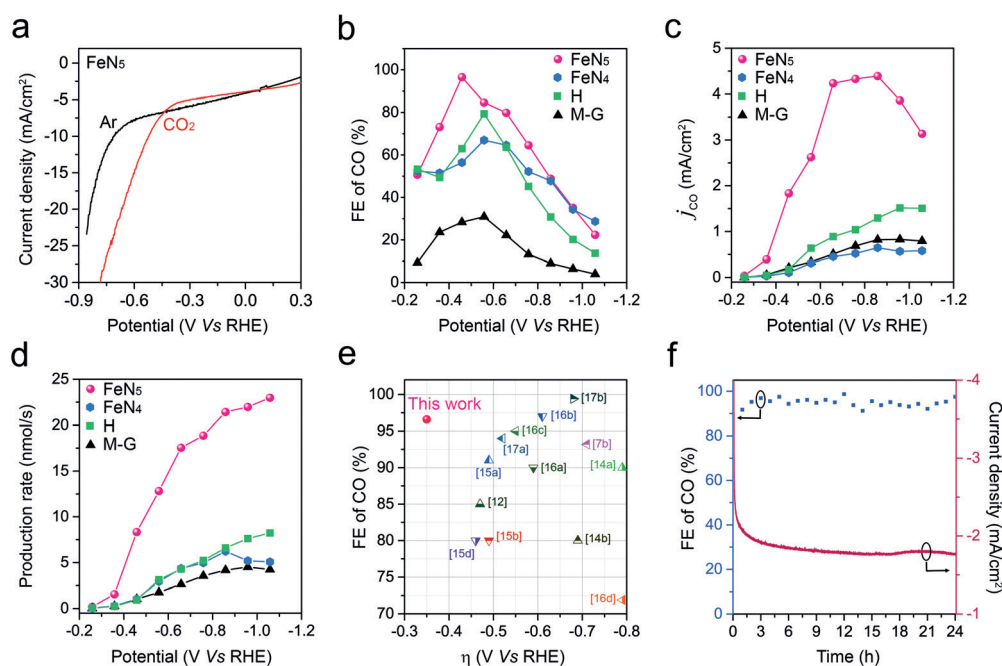
Figure 4. CO_2RR catalytic performance of as-synthesized catalysts. a) LSV scans (20 mVs^{-1}) for the FeN$_5$ catalyst (H-M-G) in Ar- and CO_2-saturated KHCO$_3$ solution (0.1 M). b–d) Comparison of the electrocatalytic activity of as-synthesized catalysts: Faradaic efficiency (b), partial current density (c), and production rate of CO versus potential (d). e) CO_2RR performance of the H-M-G catalyst in comparison with that of typical catalysts reported for CO_2RR (see Table S2). f) Long-term durability of the H-M-G catalyst operated at −0.46 V (vs. RHE) for 24 h.

catalysts tested in this study. The corresponding Faradaic efficiency (FE) for CO production was measured in the potential range from −0.26 to −1.06 V (vs. RHE) for all the catalysts synthesized. Among all these catalysts, the FeN$_5$ catalyst exhibited the highest selectivity for CO production, with a maximum FE of 97.0% at −0.46 V (vs. RHE), corresponding to an overpotential of 0.35 V. As the potential changed to more negative value, the FEs gradually decreased, since the competitive HER becomes dominant,[13] consistent with the LSV results. In comparison, the maximum FE for CO was determined to be 79, 67, and 31% for H, FeN$_4$, and M-G catalysts, respectively. The overpotential at the maximum FE for CO formation over FeN$_5$ (0.35 V) is lower than that of the FeN$_4$ and H catalysts (Figure 4b) as well as the majority of reported catalysts, including N-doped carbon matrix[12,14] and transition-metal single-atom doped carbon frameworks, such as atomic Fe,[15] atomic Ni,[7b,16] and atomic Co[17] (Figure 4e; see also Table S2). The partial current density (j_{CO}) for CO production by FeN$_5$ is also significantly higher as compared to the FeN$_4$, H, and M-G catalysts (Figure 4c). The CO production rate of the FeN$_5$ catalyst increases dramatically as the potential becomes more negative. The production rate offered by FeN$_5$ is much higher than that of other samples for all the potentials tested (Figure 4e; see also Table S2).[7b,15d,17b] The potential value affects the current density (Figure 4c) and the rate (Figure 4d) of CO formation, probably as a result of mass-transport limitations in the movement of CO_2 to the electrode and CO product from the electrode as well as the competition between HER and CO_2RR.[13,14b,18]

The excellent catalytic performance of the FeN$_5$ SAC might be ascribed to the unique electronic structure of the active site anchored on a graphene support with an enlarged specific surface area and enhanced conductivity. (see Figure S10 and Table S3).[15d] As-prepared M-G showed a much lower activity for CO_2 reduction as compared to the FeN$_5$ sample (Figure 4b), which suggests that nitrogen dopant alone is not a major contributor to the enhanced electrocatalytic performance of CO_2RR.[19] This result was further verified by a direct comparison of electrocatalytic performance between FeN$_4$ and FeN$_5$ samples. XPS results revealed that FeN$_4$ possessed a higher N and Fe content than that of FeN$_5$ (see Figure S5). However, FeN$_4$ showed much poorer electrocatalytic performance than FeN$_5$, which further indicates that the presence of the additional axial ligand in FeN$_5$ dramatically enhances the electrocatalytic CO_2RR performance.[20] Apart from its high electrocatalytic activity, we also tested the durability of the FeN$_5$ catalyst at a constant potential of −0.46 V (vs. RHE) for more than 24 h (Figure 4f). The current density showed less than 2% decay, and the FE of CO production remained constant (ca. 97%) throughout the test, thus suggesting high cycling stability of the FeN$_5$ catalyst. After long-term durability test of the FeN$_5$ catalyst, the atomic Fe remains the configuration of FeN$_5$ on the carbon matrix (see Figure S11).

To understand the superior catalytic performance of the FeN$_5$ catalyst, we calculated the free-energy profile for the lowest-energy pathway for the electrochemical CO_2-to-CO reduction on FeN$_5$ in comparison with that of FeN$_4$ (Figure 5a; see also Figure S12). The electrochemical CO_2-to-CO conversion involves two proton/electron transfer steps, including 1) the initial protonation of CO_2 to form *COOH ($CO_2 + * + H^+ + e^- \rightarrow$ *COOH); and 2) the subsequent hydrogenation of *COOH to generate *CO and H_2O (*COOH + H$^+$ + e$^- \rightarrow$ *CO + H_2O). Finally, the formed *CO can desorb from the catalyst surface to complete the catalytic process. As shown in Figure 5a, the key step for CO production is different over these two catalysts, that is, the $CO_2 \rightarrow$ *COOH step over the FeN$_5$ catalyst and the *CO desorption step over the FeN$_4$ catalyst. We noticed that the free-energy change of the key step over the FeN$_5$ catalyst is 0.77 eV ($CO_2 \rightarrow$ *COOH), which is significantly lower than that over the FeN$_4$ catalyst (1.35 eV for *CO$\rightarrow$CO + *);
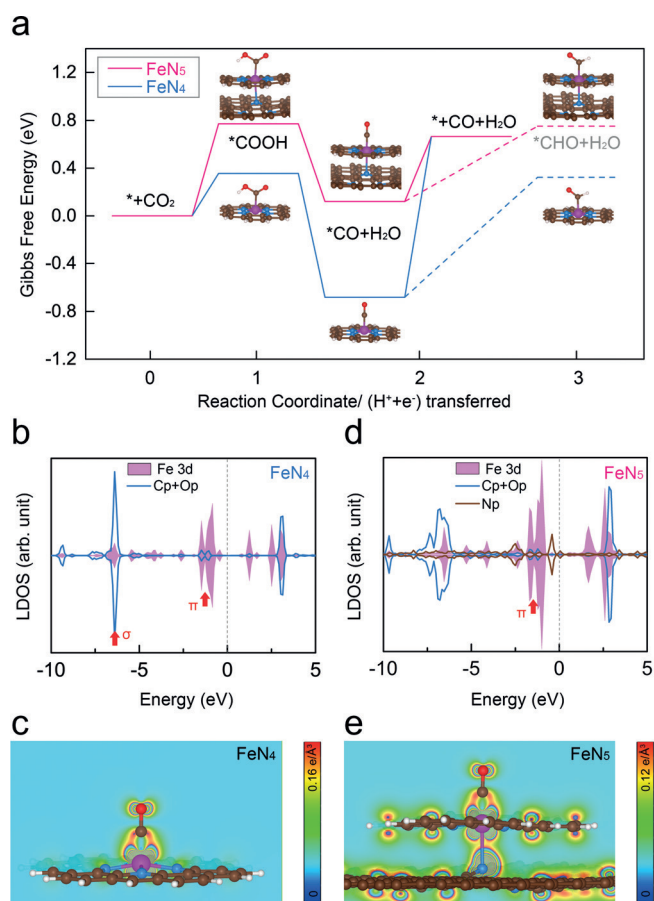
Figure 5. Evaluation of catalytic activity by DFT simulations. a) Free-energy profile with the optimized intermediates for the electroreduction of CO_2 to CO, as determined by application of the computational hydrogen electrode (CHE) model. The chemical potential of a proton–electron pair is equal to half of the chemical potential of gaseous H_2. The asterisk (*) denotes the free adsorption site, and *M (M = COOH, CO, CHO) indicates the adsorbed chemical species. b,d) Local DOS of the FeN_4 (b) and FeN_5 system (d) with adsorbed CO; the Fermi level is taken as the zero-energy point. c,e) Partial charge density of the plane formed by O-C-Fe-N within the energy range of -1.56 to -0.82 eV for FeN_4 with adsorbed CO (c) and the plane formed by O-C-Fe-N-pyrrolic N within the energy range of -3.31 to -0.99 eV for the FeN_5 system with adsorbed CO.

therefore, the FeN_5 catalyst exhibits superior catalytic activity for the CO_2-to-CO conversion. Indeed, the binding strength of *CO to the catalytic sites plays an important role in the selective CO production. As shown in Figure 5a, CO is strongly adsorbed on the FeN_4 site with a desorption energy ($\Delta G_{des} = G_{(*+CO)} - G_{(*CO)}$) of 1.35 eV, which is higher than the free-energy change for the *CO→*CHO step ($\Delta G = 1.00$ eV). Thus, it is most likely that the CO molecule will be trapped on the catalyst surface or undergo further protonation. This behavior accounts for the lower CO selectivity over the FeN_4 catalyst. In contrast, the relatively weak binding strength of *CO to the FeN_5 site ($\Delta G_{des} = 0.54$ eV) facilitates the desorption of CO from the active site, thus leading to high CO selectivity.

To gain deeper insight into the catalytic selectivity, we further investigated the local density of states (LDOS) and

partial charge density for FeN_4 with adsorbed CO (CO_FeN_4) and FeN_5 with adsorbed CO (CO_FeN_5; Figure 5 b–e; see also Figure S13). It was reported that the filled 5σ and the empty 2π* states of CO are mainly responsible for the CO–metal bonding.[21] In particular, the 2π* interaction dominates the variation of the CO binding strength, that is, the back-donation from metal d orbitals to the antibonding CO 2π* orbital strengthens the metal–carbon interaction but weakens the carbon–oxygen bond strength.[22] The σ bonding inter-action between CO and Fe of FeN_4 is located around -6.4 eV (Figure 5 b) and arises from the d_{z^2} orbital of Fe and the p_z orbitals of C and O (see also Figure S13 a). On the other hand, the CO 2π* coupling to Fe 3d states gives rise to new bonding states below the Fermi level. Partial charge density calculations in combination with the LDOS analysis (Figure 5 b,c; see also Figure S13 a) reveals that the π_{p-d} interaction is mainly due to the hybridization of Fe d_{xz}, d_{yz} orbitals and C p_x, p_y orbitals within the energy window from -1.56 to -0.82 eV. Interestingly, the interaction between Fe and the underlying pyrrolic N-doped graphene results in a unique electronic structure for the FeN_5 active site. As shown in Figure 5 d,e, the p–d coupling between pyrrolic N and Fe creates the bonding states in the energy range of -3.31 to -1.92 eV, which is lower than that of the Fe–CO π states (from -1.80 to -0.99 eV). Bader charge analysis indicated that Fe has a higher oxidation state in the FeN_5 system ($+1.19$ e) than in FeN_4 ($+0.98$ e). The d electron transferring from Fe to the p_x and p_y orbitals of the pyrrolic N atom reduces the Fe–CO π back-donation, thus leading to relatively weak CO adsorption at the FeN_5 site. Consequently, high selectivity for CO production is observed.

In summary, we have devised a new approach for the synthesis of a robust single-atom electrocatalyst consisting of atomically dispersed FeN_5 sites anchored on graphene for electrochemical CO_2 reduction. The as-synthesized FeN_5 catalyst showed excellent catalytic performance for electro-chemical CO_2-to-CO conversion with a high Faradaic effi-ciency of approximately 97.0 % at a very low overpotential of 0.35 V. In contrast to FeN_4, the axial pyrrolic N ligand depletes the electron density of Fe 3d orbitals and reduces the Fe–CO π back-donation, thus resulting in rapid CO desorp-tion for highly selective CO production. Our results pave a way for the design of novel SACs with a tunable local environment for a wide range of energy- and environment-related applications.

Acknowledgements

Conflict of interest

The authors declare no conflict of interest.

[1] a) E. V. Kondratenko, G. Mul, J. Baltrusaitis, G. O. Larrazábal, J. Pérez-Ramírez, *Energy Environ. Sci.* **2013**, *6*, 3112–3135; b) W. Zhang, Y. Hu, L. Ma, G. Zhu, Y. Wang, X. Xue, R. Chen, S. Yang, Z. Jin, *Adv. Sci.* **2018**, *5*, 1700275.

[2] a) D. D. Zhu, J. L. Liu, S. Z. Qiao, *Adv. Mater.* **2016**, *28*, 3423–3452; b) L. Zhang, Z.-J. Zhao, J. Gong, *Angew. Chem. Int. Ed.* **2017**, *56*, 11326–11353; *Angew. Chem.* **2017**, *129*, 11482–11511.

[3] a) T. Zheng, K. Jiang, H. Wang, *Adv. Mater.* **2018**, *30*, 1802066; b) C. Zhao, Y. Wang, Z. Li, W. Chen, Q. Xu, D. He, D. Xi, Q. Zhang, T. Yuan, Y. Qu, J. Yang, F. Zhou, Z. Yang, X. Wang, J. Wang, J. Luo, Y. Li, H. Duan, Y. Wu, Y. Li, *Joule* **2019**, *3*, 584–594; c) J. Shen, R. Kortlever, R. Kas, Y. Y. Birdja, O. Diaz-Morales, Y. Kwon, I. Ledezma-Yanez, K. J. P. Schouten, G. Mul, M. T. M. Koper, *Nat. Commun.* **2015**, *6*, 8177; d) R. Daiyan, X. Tan, R. Chen, W. H. Saputera, H. A. Tahini, E. Lovell, Y. H. Ng, S. C. Smith, L. Dai, X. Lu, R. Amal, *ACS Energy Lett.* **2018**, *3*, 2292–2298.

[4] a) R. Kas, K. K. Hummadi, R. Kortlever, P. de Wit, A. Milbrat, M. W. J. Luiten-Olieman, N. E. Benes, M. T. M. Koper, G. Mul, *Nat. Commun.* **2016**, *7*, 10748; b) B. Kumar, J. P. Brian, V. Atla, S. Kumari, K. A. Bertram, R. T. White, J. M. Spurgeon, *ACS Catal.* **2016**, *6*, 4739–4745.

[5] a) H. Mistry, Y.-W. Choi, A. Bagger, F. Scholten, C. S. Bonifacio, I. Sinev, N. J. Divins, I. Zegkinoglou, H. S. Jeon, K. Kisslinger, E. A. Stach, J. C. Yang, J. Rossmeisl, B. Roldan Cuenya, *Angew. Chem. Int. Ed.* **2017**, *56*, 11394–11398; *Angew. Chem.* **2017**, *129*, 11552–11556; b) S. Liu, X.-Z. Wang, H. Tao, T. Li, Q. Liu, Z. Xu, X.-Z. Fu, J.-L. Luo, *Nano Energy* **2018**, *45*, 456–462; c) Y. Yoon, A. S. Hall, Y. Surendranath, *Angew. Chem. Int. Ed.* **2016**, *55*, 15282–15286; *Angew. Chem.* **2016**, *128*, 15508–15512.

[6] a) H. Mistry, R. Reske, Z. Zeng, Z.-J. Zhao, J. Greeley, P. Strasser, B. R. Cuenya, *J. Am. Chem. Soc.* **2014**, *136*, 16473–16476; b) W. Zhu, R. Michalsky, Ö. Metin, H. Lv, S. Guo, C. J. Wright, X. Sun, A. A. Peterson, S. Sun, *J. Am. Chem. Soc.* **2013**, *135*, 16833–16836; c) Z. Cao, S. B. Zacate, X. Sun, J. Liu, E. M. Hale, W. P. Carson, S. B. Tyndall, J. Xu, X. Liu, X. Liu, C. Song, J.-h. Luo, M.-J. Cheng, X. Wen, W. Liu, *Angew. Chem. Int. Ed.* **2018**, *57*, 12675–12679; *Angew. Chem.* **2018**, *130*, 12857–12861.

[7] a) H. Zhang, J. Wang, Z. Zhao, H. Zhao, M. Cheng, A. Li, C. Wang, J. Wang, J. Wang, *Green Chem.* **2018**, *20*, 3521–3529; b) K. Jiang, S. Siahrostami, A. J. Akey, Y. Li, Z. Lu, J. Lattimer, Y. Hu, C. Stokes, M. Gangishetty, G. Chen, Y. Zhou, W. Hill, W.-B. Cai, D. Bell, K. Chan, J. K. Nørskov, Y. Cui, H. Wang, *Chem* **2017**, *3*, 950–960; c) T. Zheng, K. Jiang, N. Ta, Y. Hu, J. Zeng, J. Liu, H. Wang, *Joule* **2019**, *3*, 265–278; d) Y. Peng, B. Lu, S. Chen, *Adv. Mater.* **2018**, *30*, 1801995; e) Q. Yang, C.-C. Yang, C.-H. Lin, H.-L. Jiang, *Angew. Chem. Int. Ed.* **2019**, *58*, 3511–3515; *Angew. Chem.* **2019**, *131*, 3549–3553; f) W. Ju, A. Bagger, G.-P. Hao, A. S. Varela, I. Sinev, V. Bon, B. Roldan Cuenya, S. Kaskel, J. Rossmeisl, P. Strasser, *Nat. Commun.* **2017**, *8*, 944.

[8] a) W.-J. Jiang, L. Gu, L. Li, Y. Zhang, X. Zhang, L.-J. Zhang, J.-Q. Wang, J.-S. Hu, Z. Wei, L.-J. Wan, *J. Am. Chem. Soc.* **2016**, *138*, 3570–3578; b) H. Zhang, S. Hwang, M. Wang, Z. Feng, S. Karakalos, L. Luo, Z. Qiao, X. Xie, C. Wang, D. Su, Y. Shao, G. Wu, *J. Am. Chem. Soc.* **2017**, *139*, 14143–14149.

[9] a) Y. Chen, S. Ji, Y. Wang, J. Dong, W. Chen, Z. Li, R. Shen, L. Zheng, Z. Zhuang, D. Wang, Y. Li, *Angew. Chem. Int. Ed.* **2017**, *56*, 6937–6941; *Angew. Chem.* **2017**, *129*, 7041–7045; b) Y. Chen, S. Ji, S. Zhao, W. Chen, J. Dong, W.-C. Cheong, R. Shen, X. Wen, L. Zheng, A. I. Rykov, S. Cai, H. Tang, Z. Zhuang, C. Chen, Q. Peng, D. Wang, Y. Li, *Nat. Commun.* **2018**, *9*, 5422.

[10] Y. Xue, B. Huang, Y. Yi, Y. Guo, Z. Zuo, Y. Li, Z. Jia, H. Liu, Y. Li, *Nat. Commun.* **2018**, *9*, 1460.

[11] Y. Joly, *Phys. Rev. B* **2001**, *63*, 125120.

[12] J. Wu, M. Liu, P. P. Sharma, R. M. Yadav, L. Ma, Y. Yang, X. Zou, X.-D. Zhou, R. Vajtai, B. I. Yakobson, J. Lou, P. M. Ajayan, *Nano Lett.* **2016**, *16*, 466–470.

[13] Y. Liu, C. C. McCrory, *Nat. Commun.* **2019**, *10*, 1683.

[14] a) J. Xu, Y. Kan, R. Huang, B. Zhang, B. Wang, K.-H. Wu, Y. Lin, X. Sun, Q. Li, G. Centi, D. Su, *ChemSusChem* **2016**, *9*, 1085–1089; b) J. Wu, R. M. Yadav, M. Liu, P. P. Sharma, C. S. Tiwary, L. Ma, X. Zou, X.-D. Zhou, B. I. Yakobson, J. Lou, P. M. Ajayan, *ACS Nano* **2015**, *9*, 5364–5371.

[15] a) T. N. Huan, N. Ranjbar, G. Rousse, M. Sougrati, A. Zitolo, V. Mougel, F. Jaouen, M. Fontecave, *ACS Catal.* **2017**, *7*, 1520–1525; b) A. S. Varela, N. Ranjbar Sahraie, J. Steinberg, W. Ju, H.-S. Oh, P. Strasser, *Angew. Chem. Int. Ed.* **2015**, *54*, 10758–10762; *Angew. Chem.* **2015**, *127*, 10908–10912; c) M. Jia, Q. Fan, S. Liu, J. Qiu, Z. Sun, *Curr. Opin. Green Sustainable Chem.* **2019**, *16*, 1–6; d) C. Zhang, S. Yang, J. Wu, M. Liu, S. Yazdi, M. Ren, J. Sha, J. Zhong, K. Nie, A. S. Jalilov, Z. Li, H. Li, B. I. Yakobson, Q. Wu, E. Ringe, H. Xu, P. M. Ajayan, J. M. Tour, *Adv. Energy Mater.* **2018**, *8*, 1703487.

[16] a) P. Su, K. Iwase, S. Nakanishi, K. Hashimoto, K. Kamiya, *Small* **2016**, *12*, 6083–6089; b) H. B. Yang, S.-F. Hung, S. Liu, K. Yuan, S. Miao, L. Zhang, X. Huang, H.-Y. Wang, W. Cai, R. Chen, J. Gao, X. Yang, W. Chen, Y. Huang, H. M. Chen, C. M. Li, T. Zhang, B. Liu, *Nat. Energy* **2018**, *3*, 140–147; c) K. Jiang, S. Siahrostami, T. Zheng, Y. Hu, S. Hwang, E. Stavitski, Y. Peng, J. Dynes, M. Gangisetty, D. Su, K. Attenkofer, H. Wang, *Energy Environ. Sci.* **2018**, *11*, 893–903; d) C. Zhao, X. Dai, T. Yao, W. Chen, X. Wang, J. Wang, J. Yang, S. Wei, Y. Wu, Y. Li, *J. Am. Chem. Soc.* **2017**, *139*, 8078–8081.

[17] a) X. Wang, Z. Chen, X. Zhao, T. Yao, W. Chen, R. You, C. Zhao, G. Wu, J. Wang, W. Huang, J. Yang, X. Hong, S. Wei, Y. Wu, Y. Li, *Angew. Chem. Int. Ed.* **2018**, *57*, 1944–1948; *Angew. Chem.* **2018**, *130*, 1962–1966; b) Y. Pan, R. Lin, Y. Chen, S. Liu, W. Zhu, X. Cao, W. Chen, K. Wu, W.-C. Cheong, Y. Wang, L. Zheng, J. Luo, Y. Lin, Y. Liu, C. Liu, J. Li, Q. Lu, X. Chen, D. Wang, Q. Peng, C. Chen, Y. Li, *J. Am. Chem. Soc.* **2018**, *140*, 4218–4221.

[18] a) W. Ju, A. Bagger, G.-P. Hao, A. S. Varela, I. Sinev, V. Bon, B. R. Cuenya, S. Kaskel, J. Rossmeisl, P. Strasser, *Nat. Commun.* **2017**, *8*, 944; b) A. S. Varela, W. Ju, P. Strasser, *Adv. Energy Mater.* **2018**, *8*, 1703614.

[19] A. Zitolo, V. Goellner, V. Armel, M.-T. Sougrati, T. Mineva, L. Stievano, E. Fonda, F. Jaouen, *Nat. Mater.* **2015**, *14*, 937.

[20] R. Cao, R. Thapa, H. Kim, X. Xu, M. G. Kim, Q. Li, N. Park, M. Liu, J. Cho, *Nat. Commun.* **2013**, *4*, 2076.

[21] B. Hammer, J. K. Nørskov, *Advances in Catalysis*, Vol. 45, Academic Press, New York, **2000**, pp. 71–129.

[22] G. Blyholder, *J. Phys. Chem.* **1964**, *68*, 2772–2777.